DOI: 10.13009/EUCASS2019-503

8TH EUROPEAN CONFERENCE FOR AERONAUTICS AND AEROSPACE SCIENCES (EUCASS)

DOI: ADD DOINUMBER HERE

Role of combustion modeling in the prediction of heat transfer in LRE thrust chambers

F. Nasuti⋆†, P. Concio⋆, G. Indelicato⋆, P.E. Lapenna⋆ and F. Creta⋆
⋆Sapienza University of Rome
Dipartimento di Ingegneria Meccanica e Aerospaziale, Via Eudosssiana 18, Rome 00184, Italy
francesco.nasuti@uniroma1.it · pierluigi.concio@gmail.com · giuseppe.indelicato@uniroma1.it
pasquale.lapenna@uniroma1.it · francesco.creta@uniroma1.it ·
†Corresponding author

Abstract

The role of detailed combustion modeling and boundary layer modeling is discussed in comparison with experimental data for the seven injector GO2/GCH4 test cases developed at Technical University of Munich. Results show that unsteady Reynolds averaged Navier-Stokes equations are able to provide the evaluation of heat flux of the region close to injection plate with a reasonable agreement with experimental data. Conversely, the simplifying assumption of steady state expansion of combustion products, without detailed modeling of combustion, is confirmed to be reliable for the prediction of wall heat flux starting at 15-30 cm from injector plate.

1. Introduction

Nowadays the efforts of space industries and agencies, from the propulsion standpoint, are devoted to the development of high performance, relatively low-cost and possibly reusable liquid rocket engines (LRE). In particular, the propellant combination consisting in gaseous methane (GCH4) and liquid oxygen (LO2) has prompted significant research efforts. In this context, an important role is played by computational fluid dynamics (CFD) which is a key tool for the prediction of the complex phenomena occurring in a LRE thrust chamber. In particular, numerical simulations aiming to evaluate the wall heat loads experienced by a thrust chamber are expected to strengthen as an active support to the design process of the propulsive system. Different approaches have been considered so far to move from the basic Bartz correlation[2] and its modifications.[5] The latter is still considered as a reference provided sufficient data relevant to the engine design under development are available for a suitable calibration. Recently, CFD simulations have shown their capabilities to provide a full description of at least small scale thrust chambers.[37] This can be done at a computational cost which is not practical for design purposes, considering that it would require a huge resolution and codes able to solve at the same time combustion, boundary layer with possible finite-rate reactions, expansion up to at least sonic speed, and in some cases radiative heat flux.[21] Therefore it is worth estimating the uncertainty resulting from the different approximations that may lead to more or less affordable computations in reasonable times.

To this goal it is of great help the wealth of experimental information which has recently been obtained and made available to scientific community by a test campaign of Technical University of Munich (TUM).[9,10,33,34] Most of experimental data are relevant to the combustion chamber and have been considered as a testbench for code validation by different research groups making use of both commercial, open-source and in-house CFD software.[11,13,17,25,27,28,32]

The present work investigates on the role of combustion modeling in the evaluation of the heat transfer in the different combustion chamber regions: the injector zone, the rapid-combustion zone and the streamtube-combustion zone. Such study is carried out by comparing two different RANS modeling approaches in the simulation of the seven- injector GCH4/GO2 combustion chamber conceived and experimentally tested at the Technical University of Munich with the goal of measuring chamber heat loads.[34] The first modeling strategy aims at predicting the streamtube combustion zone and nozzle and is based on neglecting the details of the combustion process directly injecting the full mass flow rate of combustion products. It includes detailed modeling of wall processes and in particular the combustion products recombination in the near wall boundary layer by means of finite rate chemistry and a global chemical kinetic mechanism.[3] The second strategy aims at predicting the entire combustion chamber and is based on a non-adiabatic flamelet method for turbulent combustion. It employs a detailed chemical kinetic mechanism under the high Damkohler number assumption.[17] The objective of the present contribution is therefore to evaluate the differences between these

DOI: 10.13009/EUCASS2019-503

modeling approaches in terms of predictive capabilities of wall heat loads in the mentioned different regions and, eventually obtain some general insights about the modeling strategies of such class of engineering problems.

2. Test Case Description

Test case for comparison of numerical solution and experimental data has been selected among those realized at Technical University of Munich (TUM). In particular the test case featuring a seven element injector plate has been considered.[34] For both test cases propellants are gaseous methane and gaseous oxygen.

The seven-injector thrust chamber developed and tested at TUM[33] is made of four water-cooled segments of circular cross-section and a fifth segment, the nozzle, also of circular cross–section and water-cooled. The cylindrical combustion chamber includes one long and three short segments. Together with the nozzle segment the total length of thrust chamber is 341+42 mm. The combustion chamber inner diameter is 30 mm and the throat diameter is 19 mm, resulting in a contraction ratio of 2.5. In order to easily scale the chamber with the injector dimensions, the distance between the injectors as well as the injector-wall-distance are kept constant and equal to half of the injector diameter, which leads to a pattern of seven injector elements. The operating point chosen for this test case features a mean combustion chamber pressure of 18.3 bar and a mixture ratio of 2.65. With a total mass flow rate of 0.291 kg/s, this chamber features a combustion efficiency of 94.5%. The seven-element thrust chamber results to be about five times the single element one in terms of mass flow rate, thrust and throat area.

Figure 1: Geometry of seven-injector thrust chamber. Flow is from left to right.

The thrust chamber is cooled by the aforementioned two water channels. A single water channel, in fact, would not have been appropriate because of the high water temperature at the outlet of the fourth segment. For the determination of the thermal loads a calorimetric method is applied. Heating rate to each chamber segment is determined by the difference of the coolant total enthalpy between inlet and outlet. In this case thanks to the joint measure of wall temperature from thermocouples and of the heat flux for each segment from the measure of water temperature increase, information about wall temperature and heat flux are made available in the combustion chamber and a single measure of heat flux is also provided for the throat segment, which is the most relevant information for the present study.

3. Theoretical and Numerical Model

3.1 Steady RANS model with Spalart-Allmaras turbulence closure

The study of wall heat transfer in LRE thrust chambers is carried out including in principle both convection and thermal radiation models. However, based on results shown for the present test case in a study of wall heat flux at nozzle throat,[26] the radiative heat flux is negligible and therefore is not considered in the present study. The convective contribution is evaluated by the following CFD modeling.

Table 1: Reaction mechanism for oxygen/methane simulations[3] (units: cal, mol, cm, s).

j	Reaction	A_j	n_j	$E_{a,j}$, cal/mol
1	$\frac{1}{2}\,CH_4 + \frac{5}{4}\,O_2 \longrightarrow CO + 2\,H_2 + O_2$	$7.82 \cdot 10^{13}$	0.00	30000
2	$CH_4 + H_2O \longrightarrow CO + 3\,H_2$	$3.00 \cdot 10^{11}$	0.00	30000
3	$CO + H_2O \rightleftharpoons CO_2 + H_2$	$2.75 \cdot 10^{12}$	0.00	20000
4	$\frac{1}{4}\,H_2 + \frac{3}{2}\,O_2 \rightleftharpoons 2\,H_2O + \frac{1}{2}\,O_2 - \frac{7}{4}\,H_2$	$1.21 \cdot 10^{18}$	-1.00	40000
5	$O_2 \rightleftharpoons 2\,O$	$1.5 \cdot 10^{9}$	0.00	113000
6	$H_2O \rightleftharpoons H + OH$	$2.3 \cdot 10^{22}$	-3.00	120000
7	$OH + H_2 \rightleftharpoons H + H_2O$	$2.10 \cdot 10^{8}$	1.51	3430

The CFD solution is computed by solving the compressible Reynolds–averaged Navier–Stokes (RANS) equa-

DOI: 10.13009/EUCASS2019-503

tions for reacting mixtures of thermally perfect gases:[1]

$$\begin{aligned}
&\frac{\partial(\rho y_i)}{\partial t} + \nabla\cdot(\rho\mathbf{v}y_i) = -\nabla\cdot\mathbf{j}_i + \dot{\omega}_i \qquad (i = 1, ..., N_s)\\
&\frac{\partial(\rho\mathbf{v})}{\partial t} + \nabla\cdot(\rho\mathbf{v}\mathbf{v}) = \nabla\cdot\mathbf{S}\\
&\frac{\partial(\rho e_0)}{\partial t} + \nabla\cdot(\rho e_0\mathbf{v}) = \nabla\cdot(\mathbf{v}\cdot\mathbf{S}) - \nabla\cdot\mathbf{q}
\end{aligned} \tag{1}$$

The quantities under divergence sign on the right hand side of Eq. (1) are:

$$\begin{aligned}
\mathbf{j}_i &= -\left(\frac{\mu}{\mathrm{Sc}} + \frac{\mu_T}{\mathrm{Sc}_T}\right)\nabla y_i\\
\mathbf{S} &= -p\mathbf{I} - (\mu+\mu_T)\left\{\frac{2}{3}(\nabla\cdot\mathbf{v})\mathbf{I} + \left[\nabla\mathbf{v} + (\nabla\mathbf{v})^T\right]\right\}\\
\mathbf{q} &= -\left(k + \mu_T\sum_{i=1}^{N_s}\frac{y_i c_{p,i}}{\mathrm{Pr}_T}\right)\nabla T + \sum_{i=1}^{N_s}\left(h_i + \Delta h_{f,i}^{T_{ref}}\right)\mathbf{j}_i
\end{aligned} \tag{2}$$

where the value of the sensible enthalpy for the i–th species h_i, and the corresponding specific heat $c_{p,i}$ in the thermal equation of state, are expressed as a function of temperature according to the seventh–order polynomial reported for each species in Ref. 24. The standard heat of formation at the reference temperature for the i–th species $\Delta h_{f,i}^{T_{ref}}$ is also taken from.[24] The molecular transport properties μ and k are derived from those of the individual species according to Wilke's rule,[1] and those of individual species are taken from the fourth–order polynomials of temperature reported in Ref. 23. Species diffusion is considered to be the same for all species through a constant Schmidt number, assumed as Sc= 0.7. Turbulent viscosity μ_T is evaluated by the integration of an additional convection/diffusion equation, according to the Spalart–Allmaras one-equation model,[35] whose standard constants are used for model closure. Turbulent diffusivity and conductivity are evaluated on the basis of μ_T through turbulent Schmidt and Prandtl numbers, $\mathrm{Sc}_T = 0.7$ and $\mathrm{Pr}_T = 0.9$, respectively.

The chemical source terms $\dot{\omega}_i$ in Eq. (1) are obtained by the contribution of each of the N_r reactions as

$$\dot{\omega}_i = \mathcal{M}_i\sum_{j=1}^{N_r}(\nu_{i,j}^R - \nu_{i,j}^P)\left[k_{f,j}\prod_{s=1}^{N_s}\left(\frac{\rho_s}{\mathcal{M}_s}\right)^{\nu_{i,j}^R} - k_{b,j}\prod_{s=1}^{N_s}\left(\frac{\rho_s}{\mathcal{M}_s}\right)^{\nu_{i,j}^P}\right] \tag{3}$$

where the generic reaction among species B_i is expressed with stoichiometric coefficients of reactants $\nu_{i_j}^R$ and products $\nu_{i_j}^P$ as:

$$\sum_{i=1}^{N_s}\nu_{i,j}^R B_i \rightleftharpoons \sum_{i=1}^{N_s}\nu_{i,j}^P B_i \qquad (j = 1, ..., N_r) \tag{4}$$

and forward $k_{f,j}$ and backward $k_{b,j}$ reaction rates are expressed as

$$k_{f,j} = A_j\, T^{n_j}\exp\left(-\frac{E_{a_j}}{\mathcal{R}T}\right) \qquad k_{b,j} = K_j/k_{f,j} \tag{5}$$

where A_j is the pre–exponential factor, n_j the temperature exponent, E_{a_j} the molar activation energy, $\mathcal{R}$ the universal gas constant and K_j the equilibrium constant of the j–th reaction. K_j is also evaluated from thermodynamic data taken from.[24] In the present study a single reaction mechanism is used. It is an extension of the Jones–Lindstedt[15] global kinetic mechanism for an oxygen/methane mixture (Table 1), including three additional species and three extra reactions with respect to the original one with the goal of taking into account recombination reactions of dissociated species.[3]

The RANS equations are numerically integrated up to the wall by an in–house CFD solver that has been validated in different operating conditions.[3,4,6,7,20,30] The solver adopts a finite volume Godunov-type formulation. To allow the second–order accuracy in space, a linear cell reconstruction of flow variables is carried out by using the value in the considered cell and those in the contiguous ones. A Roe approximate Riemann solver[31] for multi–block structured meshes is used. This allows to evaluate variables at cell interfaces and associated fluxes to compute the evolution in time. Time integration adopts the Strang operator–splitting technique;[36] convective and diffusive terms are integrated by a second–order Runge–Kutta scheme, whereas for the chemical source term a stiff ordinary differential equation (ODE) implicit integrator is used.[8]

DOI: 10.13009/EUCASS2019-503

3.2 Unsteady RANS model with $k-\varepsilon$ turbulence closure

The solutions of the Unsteady RANS equations are obtained with the solver `RflameletSmoke`[17,18] developed in the context of the open source OpenSMOKE framework.[12] It is based on a low-Mach number approach in conjunction with a flamelet-based method for turbulent combustion modeling. Flamelet-based methods allow a detailed chemical description of the flame structure at a reasonable computational cost by means of a decomposition of the original system of equations for a reactive mixture, in a flame structure and a purely mixing problem for high Damkohler numbers. The latter allows to avoid the combustion induced stiffness of the numerical integration via the construction of a parameterized thermodynamic manifold in the form

$$\psi = \psi(Z, \chi_{st}) \tag{6}$$

being ψ a generic thermodynamic quantity of the mixture, the parameter χ_{st} the scalar dissipation rate of the mixture fraction Z at the stoichiometric value, and Z a conserved scalar measuring the local composition of the mixture ($Z = 0$ in the oxidizer stream and $Z = 1$ in the fuel one). Moreover, in the low-Mach number limit, flamelet based tabulation methods for turbulent non-premixed combustion are well-posed, and provide a properly filtered/averaged treatment of thermochemical properties.[19] An extension of the manifold in eq. 6 was originally proposed by Marracino and Lentini[22] to include non-adiabatic radiation effects in non-luminous turbulent diffusive flames, with the introduction of an enthalpy defect ϕ defined as the difference between an enthalpy $h_{ad}(Z)$ ensuing from the adiabatic and steady state solution of the flamelet equations[29] and the actual non-adiabatic enthalpy h of the flow,

$$\phi = h - h_{ad}(Z) = h - [h_O + Z(h_F - h_O)]. \tag{7}$$

being h_O and h_F respectively the enthalpy of the oxidizer and of the fuel streams. In this way non-adiabatic flamelets are computed by first calculating progressively lower enthalpy levels of the mixture from eq. 7, according to some presumed user-prescribed values of the parameter ϕ; and then by obtaining the resulting non-adiabatic flam structure, in terms of temperature and mixture composition, from the imposed enthalpy levels. All the thermo-chemistry quantities of the mixture are then evaluated according to the given thermodynamic pressure p_0 (which for the present case was set to 20 bar) and the non-adiabatic temperature and composition. In the semi-adiabatic or frozen approach, on the other hand, the mixture is subjected to non-adiabatic effects only in terms of temperature, since the composition is kept frozen to adiabatic conditions. The underlying assumption is that reaction rates vanish as the flame approaches the wall, thus preventing further reactions such as recombinations at lower enthalpies. The previously described standard defect-based model gave good results in including also wall heat loads in LRE applications, altough some limits were noticed due to the high heat loss experienced inside LRE combustion chambers.[17] In the present work a newly developed non-adiabatic flamelet model was used, whose numerical details are given in.[14]

The aforementioned solver solves transport equations for enthalpy $\widetilde{h}$ (where the symbol $\widetilde{(\ )}$ indicates that value are time averaged at a small time scale but are still function of time for variations relevant to larger time scales), mixture fraction $\widetilde{Z}$ and its variance $\widetilde{Z''}$, in addition to mass and momentum equations

$$\frac{\partial}{\partial t}(\bar{\rho} \cdot \widetilde{Z}) + \nabla \cdot (\bar{\rho}\widetilde{\mathbf{u}} \cdot \widetilde{Z}) = \nabla \cdot \left[\left(\bar{\alpha} + \frac{\bar{\rho}\nu_t}{\mathrm{Sc}_T}\right)\nabla\widetilde{Z}\right] \tag{8}$$

$$\frac{\partial}{\partial t}(\bar{\rho} \cdot \widetilde{h}) + \nabla \cdot (\bar{\rho}\widetilde{\mathbf{u}} \cdot \widetilde{h}) = \nabla \cdot \left[\left(\bar{\alpha} + \frac{\bar{\rho}\nu_t}{\mathrm{Pr}_T}\right)\nabla\widetilde{h}\right] \tag{9}$$

$$\frac{\partial}{\partial t}(\bar{\rho} \cdot \widetilde{Z''}) + \nabla \cdot (\bar{\rho}\widetilde{\mathbf{u}} \cdot \widetilde{Z''}) = \nabla \cdot \left[\left(\bar{\alpha} + \frac{\bar{\rho}\nu_t}{\mathrm{Sc}_T}\right)\nabla\widetilde{Z''}\right] + C_g\bar{\rho}\nu_t|\nabla\widetilde{z}|^2 - C_d\bar{\rho}\frac{\widetilde{\epsilon}}{\widetilde{k}} \cdot \widetilde{Z''} \tag{10}$$

being $\bar{\rho}$ the Reynolds averaged density coming from the tabulated flamelets, ν_t the turbulent viscosity calculated from the standard $k-\epsilon$ turbulence closure model,

$$\nu_t = C_\mu \frac{\widetilde{k}^2}{\widetilde{\epsilon}} \tag{11}$$

Pr_T and Sc_T the Prandtl and Schmidt turbulent numbers set to 0.895 and 0.85 respectively, C_g, C_d and C_μ model constants equal to 2.86, 2.00 and 0.09 respectively. The pressure-velocity coupling is handled with the PIMPLE operator splitting algorithm. The computational domain is discretized with a Gauss-Seidel finite volume method in a block-structured grid, second and first order accurate in space and time, respectively. The thrust chamber nozzle is not considered because of the low-Mach number assumptions. Wall functions are used for the turbulent quantities at wall, such as turbulent viscosity, thermal diffusivity, kinetic energy and turbulent dissipation, according to the formulation proposed in Ref. 16.

DOI: 10.13009/EUCASS2019-503

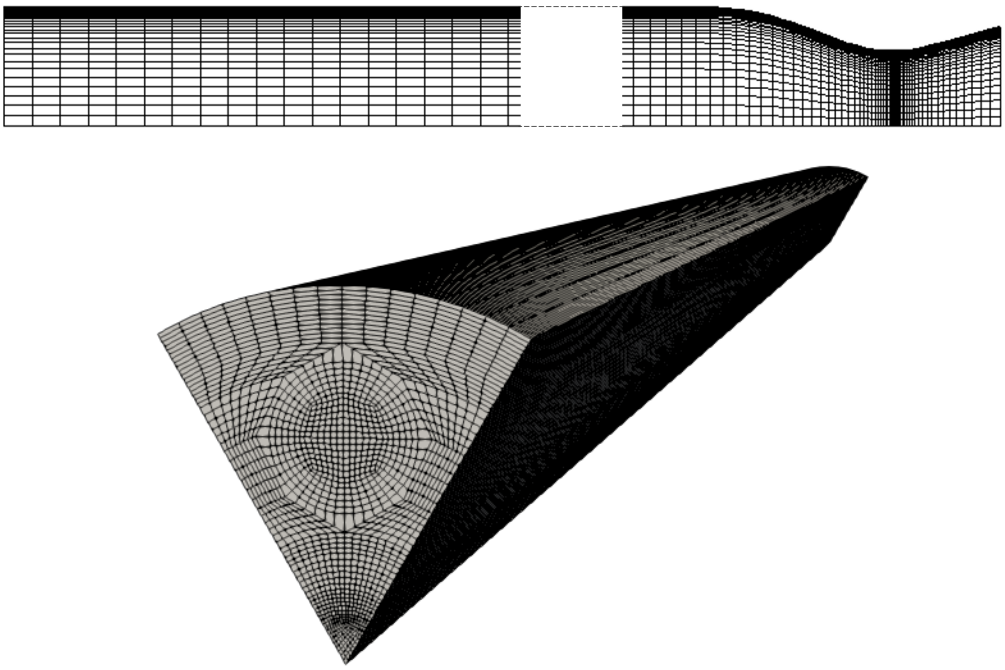

Figure 2: Computational grid: RANS (top) and URANS (bottom).

4. Results

Results obtained with the two different approaches are presented in this section. The first part discusses the present numerical results in comparison with experimental data. The second part presents a discussion of details of each numerical solution as compared with the others. The simulations are characterized by different assumptions and grid resolutions (see Fig. 2). The URANS Simulation is carried out in the first 30 cm of the cylindrical part of the thrust chamber. The structured grid used for the simulation is made of 183000 cells, distributed as 16 equispaced cells in the azimuthal direction, 128 along the chamber axis and 64 along the chamber radius. A longitudinal grading of 20 is imposed, resulting in a maximum cell length at the end of the chamber of 7 mm. Wall functions are used to solve the boundary layer. Because of this the width of the last cell before the upper wall is 3.5 mm resulting in a mean $y+$ value of about 400 all over the chamber wall. Boundary conditions are: mass flow rate and temperature at the inlet of each injector, isothermal wall at walls (temperature is an average temperature of experimental data) except for the plate and the post-tip wall where adiabatic conditions are enforced, and static pressure at the chamber end.

The steady RANS simulation includes a longer domain in the axial direction, and especially, as it is able to solve compressible flows, it also includes nozzle throat. On the other hand, no simulation of the combustion process is included. Solution is obtained over a two-dimensional grid with the assumption of axisymmetric flow. The structured grid includes 9600 cells clustered at walls (such to have the first cell center at a nondimensional turbulence wall distance $y+$ 1 all along the thrust chamber) and at throat. Governing equations are solved up to the wall. Boundary conditions assume that the total temperature and pressure, as well as composition at inlet are known. Moreover, isothermal no-slip wall is assumed with wall temperature taken from average values of the measured data.

4.1 Comparison with experimental data

The available experimental data to be compared with numerical results are the following: i) the overall heat transferred from the hot gas to water for each segment; and ii) the pressure evolution along the thrust chamber.

Pressure changes along the chamber mainly occurs because of the combustion process. Therefore as shown in Fig. 3, the solution obtained with the steady RANS approach only shows a slight decrease due to friction. On the other hand the comparison of the pressure evolution for the URANS approach, which includes combustion, shows a good agreement with the increasing/decreasing trend of experimental data. In fact, the good prediction of position and amount of pressure changes along the chamber shows that the combustion process is well captured by the numerical code. Note that, the different modeling aimed to improve the wall heat flux prediction (see “non-adiabatic”, “semi-

DOI: 10.13009/EUCASS2019-503

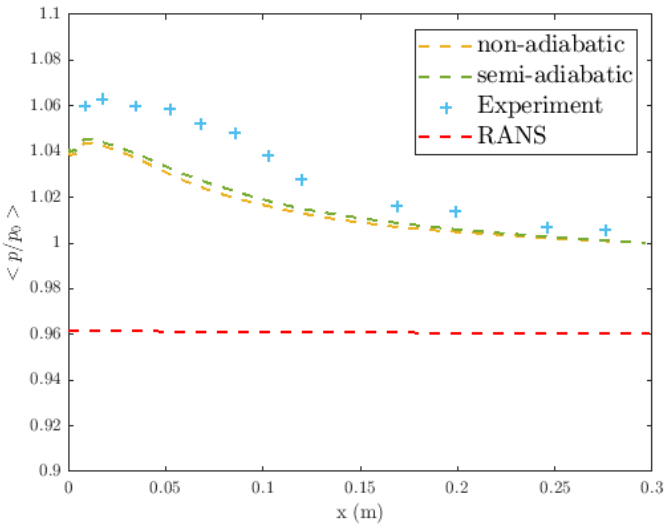

Figure 3: Wall pressure behavior along the chamber compared with experimental.[27]

adiabatic" and "adiabatic" flamelet) does not affect the quality of the combustion process prediction. Is to be noted that, in Fig. 3, the RANS and URANS pressure profiles are normalized with respect to the nominal pressure at which the chamber operates, which for the URANS simulation is 20 bar and for the RANS 18.3 bar.

Given the goal of the present paper, the most significant comparison is that of the computed heat fluxes. For a

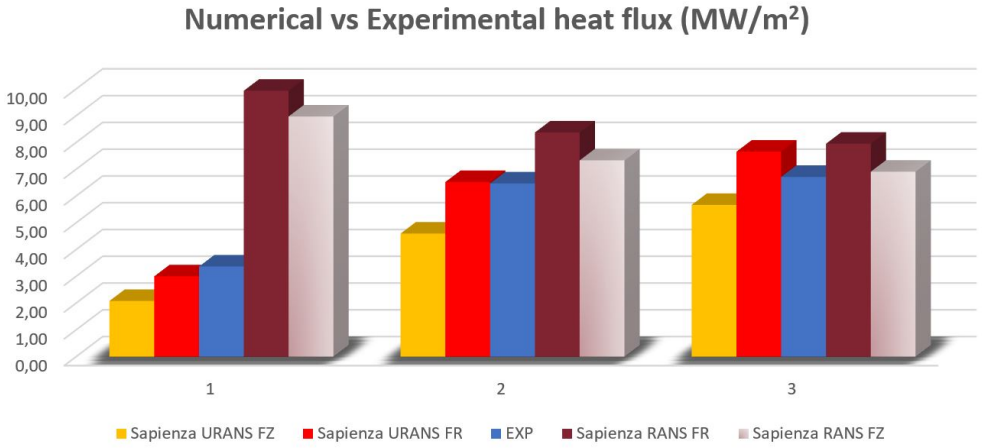

Figure 4: Computed (*Sapienza*) and experimental[27] heat flux at each segment.

correct comparison the first three segments are considered, where both steady RANS and URANS simulations have been considered. For the results relevant to the throat heat flux prediction with the RANS approach a wider discussion has been already presented.[26] In Fig. 4 four solutions are compared with experimental data for each of the three segments. The experimental value of heat flux has been obtained on the basis of the overall heat transferred to the cooling water within the segment. To be compared with experimental data for RANS equations the value shown in the figure is the space-averaged value along the exposed wall surface of the segment (heat power divided by area). For the URANS computations heat flux is both spatially and temporally averaged (overall heat divided by time and area). Expectedly, the values obtained in the first two segments with the RANS code, which evolves combustion products, provides results quite higher than experimental data. On the other hand, results obtained with the detailed simulation of the combustion process by the URANS solver is able to capture the increasing trend of heat flux. It can be noted that of the two solutions obtained with URANS code, the one which better approximate the experimental data considers reactions within the boundary layer. The increase of wall heat flux due to recombination reactions in the vicinity of the wall is also shown by the RANS solution. It is interesting to underline that RANS and URANS solutions are quite close to each other in the third segment, both slightly overestimating the experimental data.

DOI: 10.13009/EUCASS2019-503

4.2 Code to code comparison

Once the solutions have been compared with experimental data it is worth to discuss the limits and possibilities given by each of them exploiting the availability of a richer modeling from URANS solutions to estimate the uncertainties resulting from the simplified RANS approach. It has been shown that neglecting chemical reactions of recombination in the boundary layer reduces significantly the resulting wall heat flux and therefore cannot be accepted as a reliable approach. Accordingly, only solutions obtained including chemical recombinations at wall will be compared in the following. The detailed heat flux evolution is compared first in Fig. 5. The increasing trend resulting from the ad-

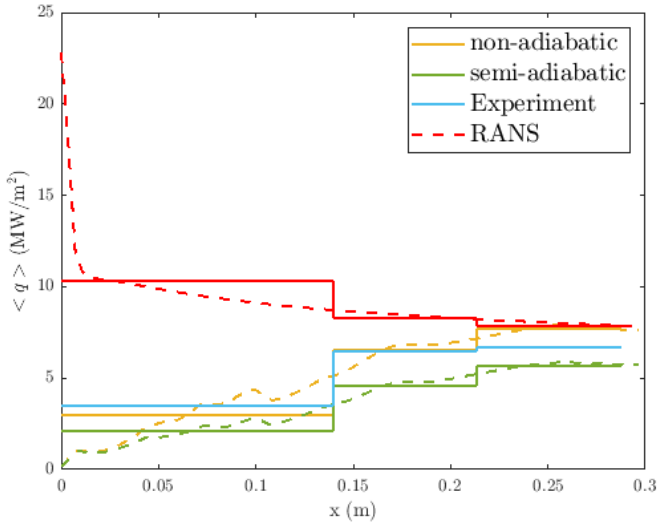

Figure 5: Comparison of wall heat flux evolution obtained with different numerical modeling.

vancement of the combustion process flattens at about 15 cm from the injector plate and start decreasing at a distance of 25 cm. This latter trend fits reasonably well with that of steady RANS evolution of combustion products mixture, showing that the approximation begins to be reliable for the heat flux prediction at that distance from the injector plate. Nevertheless, it is clear that the evolution to reach a similar heat flux level is quite different and therefore more details about the flow conditions along the thrust chamber have to be compared.

The first quantities to be investigated are those which mainly affect heat flux. Therefore, the comparison should address first the total temperature which is to be the main driver for the heat flux. However, because of the low velocity of the flow the computed static temperature evolution is shown in Fig. 6 It can be observed that a little decrease of energy content due to cooling occurs and can be detected in the RANS case where no energy addition is provided by combustion processes in the computational domain. The 2D fields of the time-averaged temperature for the URANS simulation reported in Fig. 6 are extracted from longitudinal slices along the chamber at 0 and 30 degree, where the former corresponds to the middle plane of the chamber and the latter to the symmetry plane of the simulated geometry (see Fig. 2). It can be observed that, in the middle plane slice, the flames envelope the two cold gaseous oxygen streams emanating from the central and the outer injector, while only the central jet is observed in the plane extracted at 30 degree due to three-dimensional effects.

The differences in the temperature fields are further investigated in Fig. 7 by sampling radial temperature profiles for the RANS and URANS simulations at two sections along the chamber axis, namely at $x = 10$ cm and 30 cm. The solutions at $x = 10$ cm highlight the qualitative difference between the RANS and the URANS simulations due to injection conditions: in the former in fact the full-flow assumption is employed thus neglecting detailed injection phenomena and so the flames shape, clearly visible in the URANS results. These differences can be seen on both the temperature and the species radial profiles for the CO_2 and the H_2O. Note that comparing the maximum temperature values attained in correspondence of the flames locations, their difference can be as high as almost 330 K. Differences are significantly reduced as attention is focused downstream at $x = 30$ cm (Fig. 8). Looking at the same profiles taken at $x = 30$ cm, the differences are smaller due to the increased mixedness achieved (see Fig. 6).

In Fig. 9 is reported the two-dimensional field of the H_2O mass fractions obtained with RANS and URANS simulations for further comparison. For the URANS simulation, it is obtained from a longitudinal slice as a representative comparison with the results seen before in Fig. 9. As we can see the recombinations at wall are captured and are in good agreement with the field of the RANS simulation, especially in the second half of the chamber.

DOI: 10.13009/EUCASS2019-503

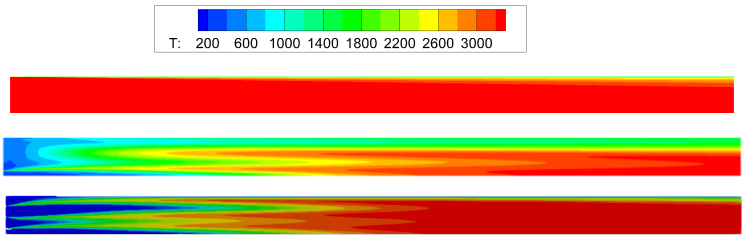

Figure 6: Comparison of temperature fields obtained with different numerical modeling: steady RANS (top); URANS lateral symmetry plane (middle); URANS central symmetry plane (bottom)

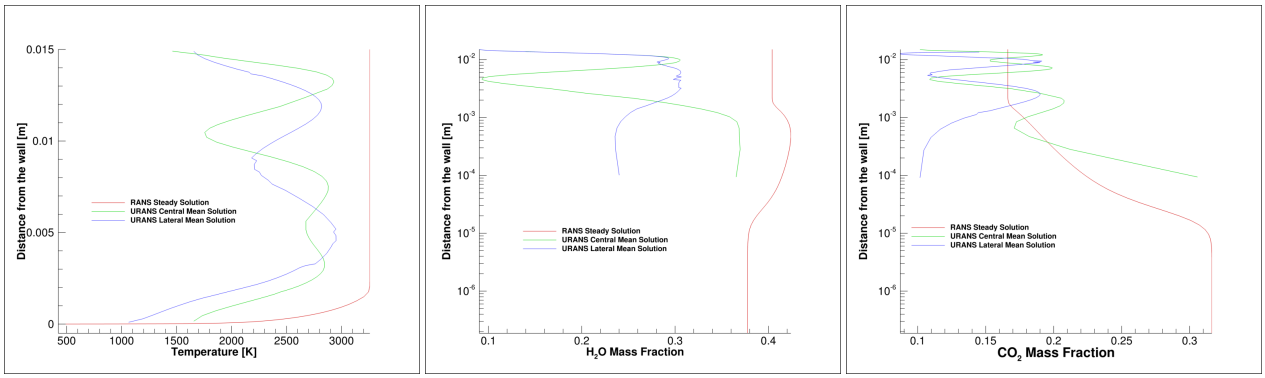

Figure 7: Radial profiles for temperature (left), H_2O mass fraction (center) and CO_2 mass fraction (right) at $x = 10$ cm for the RANS and the URANS simulation. For the latter, reported are the radial profiles sampled at 0 (green line) and 30 degree (blue line).

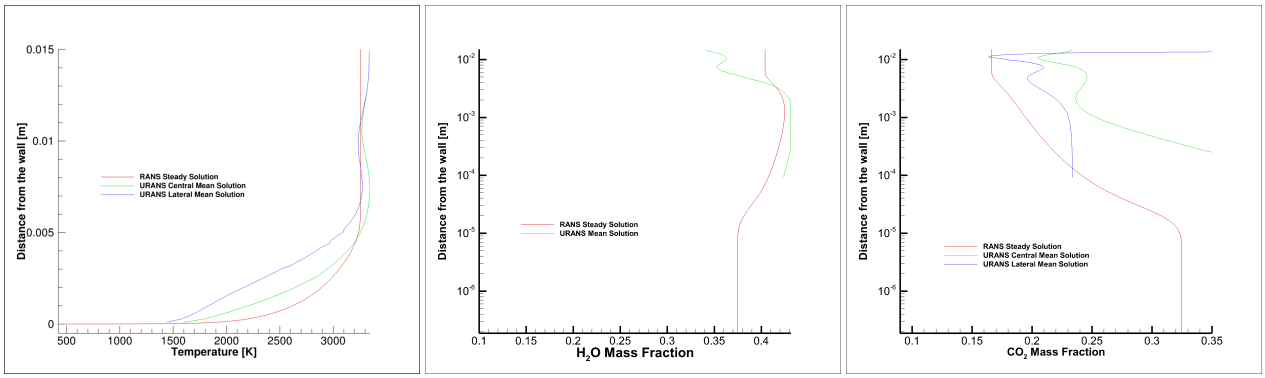

Figure 8: Radial profiles for temperature (left), H_2O mass fraction (center) and CO_2 mass fraction (right) at $x = 30$ cm for the RANS and the URANS simulation. For the latter, reported are the radial profiles sampled at 0 (green line) and 30 degree (blue line).

5. Conclusions

The comparison of the solutions obtained including or not the details of the combustion process via different URANS and RANS approaches, has shown that for the present test case suitable modeling allows to reproduce the experimental data with reasonable accuracy. In particular, it has been shown that with a detailed modeling of the combustion process, a URANS model based on a low-Mach number approach in conjunction with a flamelet-based method for turbulent combustion modeling provides a good compromise between accuracy of prediction and computational cost. On the other hand, for large scale engines and especially when the interest is focused on the evaluation of heat flux in the converging diverging nozzle, a RANS approach based on the injection of combustion products at inlet show to be the best compromise. The latter statement is confirmed by the good agreement of RANS solution with the URANS

DOI: 10.13009/EUCASS2019-503

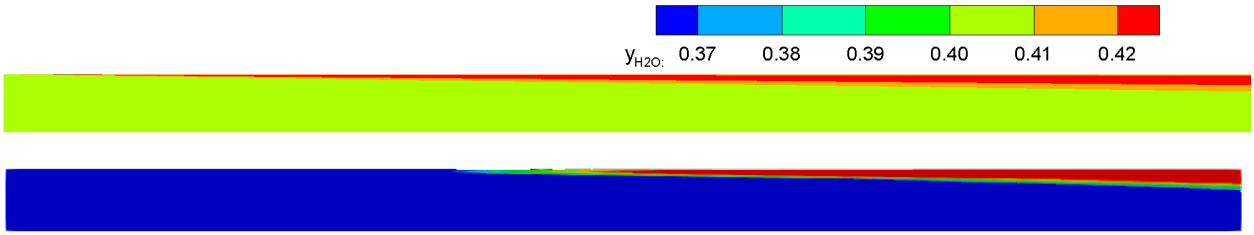

Figure 9: Comparison of H_2O mass fraction fields obtained with different numerical modeling: steady RANS (top); URANS (bottom)

solution and experimental data at the ending part of the cylindrical part of the combustion chamber.

References

[1] J. D. Anderson. *Hypersonic and High-Temperature Gas Dynamics*, pages 596–617. AIAA Education series, Reston, VA, 2006.

[2] D. R. Bartz. A simple equation for rapid estimation of rocket nozzle convective heat transfer coefficients. *Jet Propulsion*, 27(1):49–53, 1957.

[3] B. Betti, D. Bianchi, F. Nasuti, and E. Martelli. Chemical reaction effects on heat loads of CH_4/O_2 and H_2/O_2 rockets. *AIAA Journal*, 54(5):1693–1703, May 2016. doi:10.2514/1.J054606.

[4] B. Betti, M. Pizzarelli, and F. Nasuti. Coupled heat transfer analysis in regeneratively cooled thrust chambers. *Journal of Propulsion and Power*, 30(2):360–367, 2014. doi:10.2514/1.B34855.

[5] Barbara Betti, Daniele Liuzzi, Francesco Nasuti, and Marcello Onofri. Development of heat transfer correlations for LOX/CH4 thrust chambers. In *Proceedings of 6th European Conference for Aeronautics and Space Sciences*. EUCASS.

[6] D. Bianchi, B. Betti, F. Nasuti, and C. Carmicino. Simulation of gaseous oxygen/hydroxyl-terminated polybutadiene hybrid rocket flowfields and comparison with experiments. *Journal of Propulsion and Power*, 31(3):919–929, 2015. doi:10.2514/1.B35587.

[7] D. Bianchi, F. Nasuti, and C. Carmicino. Hybrid rockets with axial injector: Port diameter effect on fuel regression rate. *Journal of Propulsion and Power*, 32(4):984–996, 2016. doi:10.2514/1.B36000.

[8] P. N. Brown, G. D. Byrne, and A. C. Hindmarsh. Vode: A variable-coefficient ode solver. *SIAM Journal on Scientific and Statistical Computing*, 10(5):1038–1051, 1989. doi:10.1137/0910062.

[9] M. P. Celano, S. Silvestri, C. Bauer, N. Perakis, G. Schlieben, and O. J. Haidn. Comparison of single and multi-injector GOX/CH4 combustion chambers. AIAA Paper 2016-4990, 2016.

[10] M. P. Celano, S. Silvestri, G. Schlieben, C. Kirchberger, O. Haidn, and O. Knab. Injector characterization for a gaseous oxygen-methane single element combustion chamber. In *Progress in Propulsion Physics*, volume 8, pages 145–164, 2016.

[11] A. Chemnitz, T. Sattelmayer, C. Roth, O. Haidn, Y. Daimon, R. Keller, P. Gerlinger, J. Zips, and M. Pfitzner. Numerical investigation of reacting flow in a methane rocket combustor: Turbulence modeling. *Journal of Propulsion and Power*, 34:864–877, 2018.

[12] Alberto Cuoci, Alessio Frassoldati, T Faravelli, and Eliseo Ranzi. Opensmoke++: An object-oriented framework for the numerical modeling of reactive systems with detailed kinetic mechanisms. *Computer Physics Communications*, 192:237–264, 2015.

[13] Y. Daimon, H. Negishi, S. Silvestri, , and O. J. Haidn. Conjugated combustion and heat transfer simulation for a 7 element GOX/GCH4 rocket combustor. AIAA Paper 2018-4553, 2018.

DOI: 10.13009/EUCASS2019-503

[14] Giuseppe Indelicato, Pasquale Lapenna, Diego Durigon, and Francesco Creta. Simulations of turbulent combustion and wall heat transfer in single and multi injectors gch4/gox rocket combustors. In *Proceedings of 8th European Conference for Aeronautics and Space Sciences*. EUCASS.

[15] W. P. Jones and R. P. Lindstedt. Global reaction schemes for hydrocarbon combustion. *Combustion and Flame*, 73(3):233–249, September 1988. doi:10.1016/0010-2180(88)90021-1.

[16] Georgi Kalitzin, Gorazd Medic, Gianluca Iaccarino, and Paul Durbin. Near-wall behavior of ransturbulence models and implications for wall functions. *Computational physics*, 204(205):23–48, 2004.

[17] P. Lapenna, R. Amaduzzi, D. Durigon, G. Indelicato, F. Nasuti, and F. Creta. Simulation of a single-element gch4/gox rocket combustor using non-adiabatic flamelet method. AIAA Paper 2018-4872, 2018.

[18] P. E. Lapenna, G. Indelicato, R. Lamioni, and F. Creta. Modeling the equations of state using a flamelet approach in lre-like conditions. *ACTA Astronautica*, 2018.

[19] Pasquale Eduardo Lapenna and Francesco Creta. Mixing under transcritical conditions: an a-priori study using direct numerical simulation. *The Journal of Supercritical Fluids*, in press, 2017.

[20] G. Leccese, D. Bianchi, B. Betti, D. Lentini, and F. Nasuti. Convective and radiative wall heat transfer in liquid rocket thrust chambers. *Journal of Propulsion and Power*, 34(2):318–326, 2018. doi:10.2514/1.B36589.

[21] G. Leccese, D. Bianchi, B. Betti, D. Lentini, and F. Nasuti. Numerical investigation on radiative heat loads in liquid rocket thrust chambers. *Journal of Propulsion and Power*, 2019.

[22] B. Marracino and D. Lentini. Radiation modelling in non-luminous nonpremixed turbulent flames. *Combustion Science and Technology*, 128:23–48, 1997.

[23] B. J. McBride and S. Gordon. Computer program for calculation of complex chemical equilibrium compositions and applications. NASA RP-1311, 1994.

[24] B. J. McBride, M. J. Zehe, and S. Gordon. Nasa glenn coefficients for calculating thermodynamic properties of individual species. Technical Report NASA/TP–2002–211556, September 2002.

[25] H. Muller, J. Zips, M. Pfitzner, D. Maestro, B. Cuenot, S. Menon, R. Ranjan, P. Tudisco, and L. Selle. Numerical investigation of flow and combustion in a single-element gch4/gox rocket combustor: A comparative les study. AIAA Paper 2016-4997, 2016.

[26] F. Nasuti, M. L. Frezzotti, and P. Concio. Numerical estimation of peak heat flux at throat of liquid rocket engines. In *Proceedings of the Joint Symposium 32nd ISTS and 9th NSAT*, Fukui, Japan, 2019.

[27] N. Perakis, O. J. Haidn, D. Eiringhaus, D. Rahn, S. Zhang, Y. Daimon, S. Karl, and T. Horchler. Qualitative and quantitative comparison of rans simulation results for a 7-element gox/gch4 rocket combustor. AIAA Paper 2018-4556, 2018.

[28] N. Perakis, D. Rahn, D. Eiringhaus, and O. Haidn. Heat transfer and combustion simulation of a 7-element gox/gch4 rocket combustor. AIAA Paper 2018-4554, 2018.

[29] N. Peters. *Turbulent Combustion*. Cambridge University Press, UK, Cambridge, UK, 2000.

[30] M. Pizzarelli, F. Nasuti, R. Paciorri, and M. Onofri. Numerical analysis of three-dimensional flow of supercritical fluid in cooling channels. *AIAA Journal*, 47(11):2534–2543, November 2009. doi:10.2514/1.38542.

[31] P. L. Roe. Approximate Riemann solvers, parameter vectors and difference schemes. *Journal of Computational Physics*, 43:357–372, 1981. doi:10.1016/0021-9991(81)90128-5.

[32] C. M. Roth, O. Haidn, A. Chemnitz, T. Sattelmayer, G. Frank, H. MÃ¼ller, J. Zips, R. Keller, P. M. Gerlinger, D. Maestro, C. Benedicte, H. Riedmann, and L. Selle. Numerical investigation of flow and combustion in a single-element gch4/gox rocket combustor. AIAA Paper 2016-4995, 2016.

[33] S. Silvestri, C. Bauer, P. Lungu, and O. J. Haidn. Axial and azimuthal heat load distribution in 7-injector gox/gch4 combustion chamber. AIAA Paper 2018-4552, 2018.

[34] S. Silvestri, M. P. Celano, G. Schlieben, and O. J. Haidn. Characterization of a multi-injector gox/ch4 combustion chamber. AIAA Paper 2016-4992, 2016.

DOI: 10.13009/EUCASS2019-503

[35] P. R. Spalart and S. R. Allmaras. A one–equation turbulence model for aerodynamic flow. *La Recherche Aèrospatiale*, 1:5–21, 1994.

[36] G. Strang. On the construction and comparison of difference schemes. *SIAM Journal on Numerical Analysis*, 5:506–517, September 1968. doi:10.1137/0705041.

[37] A. Urbano, L. Selle, G. Staffelbach, B. Cuenot, T. Schmitt, S. Ducruix, and S. Candel. Exploration of combustion instability triggering using large eddy simulation of a multiple injector liquid rocket engine. *Combustion and Flame*, 169:129–140, July 2016. doi:10.1016/j.combustflame.2016.03.020.